

# Distinguish the EMRI and B-EMRI system by gravitational waves

Kun Meng<sup>1\*</sup>, Hongsheng Zhang<sup>2†</sup>, Xi-Long Fan<sup>3‡</sup>, Yuan Yong<sup>3</sup>

<sup>1</sup>School of Physics and Electronic Information, Weifang University, Weifang 261061, China

<sup>2</sup>School of Physics and Technology, University of Jinan, Jinan, China

<sup>3</sup>School of Physics and Technology, Wuhan University, Wuhan, Hubei 430072, China

May 14, 2024

## Abstract

Binary stars are as frequency as single stars in the Universe, and at least 70% of the massive stars located in our Galaxy belong to a binary system. For the first time we produce the gravitational waveforms for the extreme mass ratio inspiral systems (EMRIs) of binary stars moving around central supermassive black hole (SBH). We calculate the orbits of such systems via the Hamilton-Jacobi approach. To improve accuracy we adopt the quadrupole-octupole expression of gravitational wave (GW) and consider the contribution of radiation reaction. Compared to the waveforms of single star, double or multiple spikes emerge in the waveforms of binary stars. We calculate the mismatch of the EMRI waveforms of binary stars and those of single stars, and find the mismatch increases as the binary internal semi-latus rectum  $\tilde{p}$  decreases. According to the distinguishable criterion of two signals, it's inferred that the two types of waveforms are distinguishable for small enough  $\tilde{p}$ . Further, we demonstrate that the most favourable position to distinguish the waveforms of EMRIs of single star from the waveforms of EMRIs of binary stars is that revolutions of the binary stars and the central SBH takes the same direction, i.e., the rotation axis of the binary is parallel to that of the central SBH.

## 1 Introduction

Black hole (BH) may be the most thoroughly-studied object before its discovery in the history of science. Recently, the Event Horizon Telescope (EHT) collaboration announced the images of the SBHs M87\* and SgrA\* [1, 2], these discoveries together with the detections of GWs [3, 4] confirm the existence of black holes, and launch a new era of testing gravity in strong-field regime and far beyond the scale of solar system.

The goal of next generation GW detector—Laser Interferometer Space Antenna (LISA)—is designed to be most sensitive to detect low frequency GW signals in the band about  $10^{-4} - 1$  Hz. Taiji and Tianqin are designed to probe GWs at similar band. EMRIs are the sources generating GWs in this band. EMRIs are composed of central SBH and stellar-mass compact objects moving around the SBH. The multi-body interaction in the cusp of the stellar population surrounding the SBH may scatter the compact objects into the orbits close the central SBH and form the EMRIs [5, 6]. The GWs generated by EMRIs carry the information both of the background BH and the stellar-mass compact objects, so detections of GWs will help to learn more about the the strong-field character of the BH spacetime, the multipole structure of the BH, the structures of the small body compact objects, and the information of the underlying theory governing the way in which our universe works.

Analysis of the data released by GW detectors replies heavily on the matched filtering technique, which makes correlations between data and template waveforms, thus data analysis require establishing the template waveforms of EMRIs.

The waveforms generated by motions of single stellar-mass compact object in BH spacetime have been studied intensively [7–24], including probe fundamental fields [25, 26], modified gravity [27–32], extra dimensions [33], electric charge and internal structure of small body objects [34–40], etc. Binary-star systems are important astrophysical objects which are constituted of binary stars revolving around each other. The amount of binary-star systems is

---

\*kunmeng@wfu.edu.cn

†sps\_zhanghs@ujn.edu.cn

‡xilong.fan@whu.edu.cn

huge in the Galaxy, it's estimated that the amount of binary-star systems is no less than that of single star. The vast majority of stars are located in a binary system. It is estimated that more than 70% of all massive stars may exist in systems with two or three stars. In active galactic nuclei, due to the rich forms of interactions between SBH, the gaseous accretion disks and the stellar mass compact objects, the binary may be formed and scattered onto the orbits close the central SBH to form the systems which we call B-EMRIs. The binary stars moving in central SBH constitute a significant typical EMIRs. Thus, it is quite sensible to consider the waveforms produced by motions of binary stars surrounding a SBH other than the case of single star. The GW generated by each of the binary star overlaps, so the waveforms generated by this type of EMRIs are distinguishable from that generated by single star. In this paper, we just consider the case that the amplitudes of the GW generated by internal motion of binary stars are small compared to that generated by external motion of the mass center, so it's expected small perturbations would appear when compared to the waveforms of single star. It's really worthwhile to build the template waveforms of such systems for future data analysis to distinguish the waveforms of the binary-star systems and that of single star.

Since the traditional method of calculating gravitational waveforms—solving Teukolsky equations—cost a lot of time and computational resources [41–53], while realistic data analysis need to handle a large number of waveforms, thus more practical methods are needed. In this paper, we adopt the “numerical kludge” (NK) method which generates waveforms more conveniently and quickly but captures the principle feature of true waveforms [54]. To improve accuracy, aside from the mass quadrupole we take into account the mass octupole and current quadrupole moments of the source to solve the wave equations. It's justified the NK method does excellently at approximating the true gravitational waveforms so this method has already been used for scoping out data analysis of LISA. For the radiation reaction, we consider the adiabatic evolution of orbit parameters: the timescale of evolution of the orbit parameters is much larger than that of orbit cycles such that the motion of mass point in BH spacetime is nearly geodesic. Further, since the amplitude of GWs generated by internal motions are small compared to that generated by external motions of the mass center, to simplify the question we only consider the radiation reaction due to the GW emissions generated by the motion of mass center. We take the hybrid scheme that combines Tagoshi's [46], Shibata's [53] and Ryan's fluxes [55, 56], which performs well for generic circular-inclined orbits when compared to Teukolsky-based results [57].

The paper is organised as follows. In section 2 we calculate the trajectories of the binary stars and give waveforms of GW with the NK method. In section 3 we analyse the waveforms by calculating mismatch between the waveforms of binary stars and that of single star. We summarize our results in the last section. In this work, we adopt the geometrized units with  $G = c = 1$ .

## 2 Numerical Kludge Waveforms

In this section we adopt the NK waveforms approach developed in [54] to produce the GW waveforms of the B-EMRIs. We consider the system as, the central SBH is Kerr, the stellar-mass binary stars revolve around each other and they as a whole move along the inspiral trajectory of the central SBH. The binary stars are supposed to live far away from the SBH such that the internal gravity between them dominates, so the impacts of the SBH on the internal orbit of the binary stars are neglected, while the center of mass of the binary stars is still on the inspiral trajectory of the SBH. The geometry of binary stars moving in the spacetime of SBH is illustrated in Fig.1.

### 2.1 the geometry of the orbit

The binary are supposed to revolve around each other along elliptic orbit. We introduce the relative coordinates  $\vec{r} = \vec{r}_1 - \vec{r}_2$ , with  $\tilde{r} = \frac{\tilde{p}}{1 + \tilde{e} \cos \tilde{\beta}}$ , then the coordinates of the binary with masses  $m_1$  and  $m_2$  can be expressed with coordinates of mass center and relative coordinates as  $\vec{r}_1 = \vec{r}_C + \vec{\tilde{r}}_1, \vec{r}_2 = \vec{r}_C + \vec{\tilde{r}}_2$ , where  $\vec{\tilde{r}}_1 = \frac{m_1}{m_1 + m_2} \vec{\tilde{r}}, \vec{\tilde{r}}_2 = -\frac{m_2}{m_1 + m_2} \vec{\tilde{r}}$ . We use the coordinates and parameters with tilde to describe the internal motion of binary stars around each other. The spin axis of the central SBH is along  $z_0$ , as displayed in Fig.1,  $\theta_0$  is the angle between  $z_0$  and  $z$  which is the normal direction of the surface of binary stars' internal elliptic orbit.  $\phi_0$  is the angle between  $x_0$  and the node line which is the intersection line between the surface of binary stars' internal orbit and the horizontal surface.

Now let's discuss the orbit of a mass point in Kerr spacetime, in Boyer-Lindquist coordinates Kerr metric can

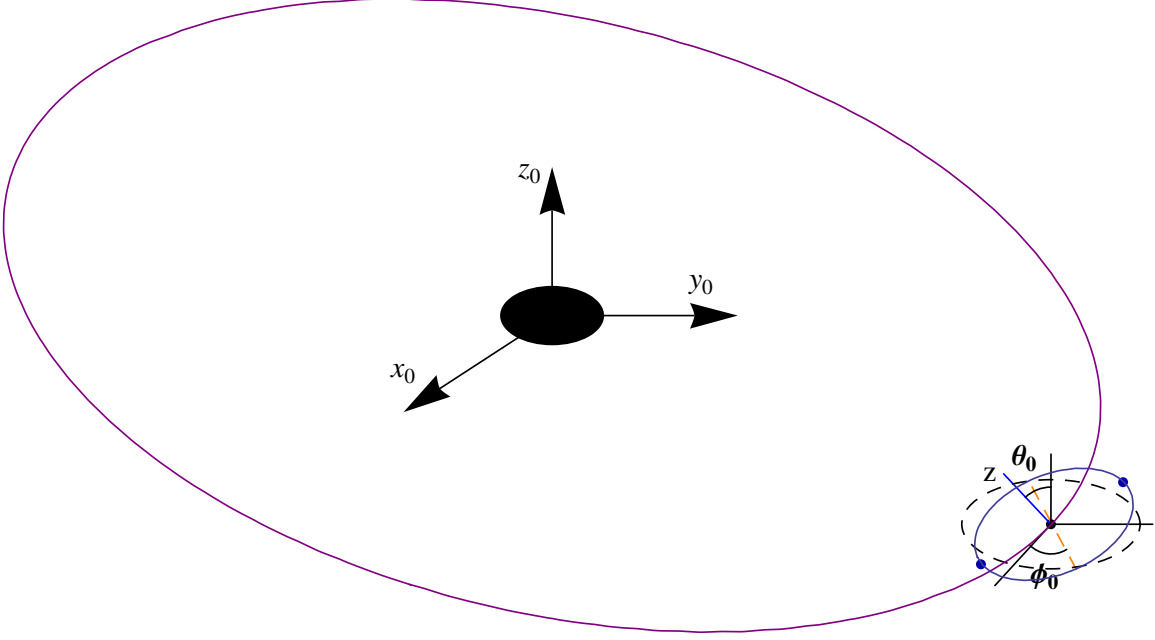


Figure 1: The geometry of binary stars orbiting around the central SBH.

be expressed as

$$ds^2 = - \left( 1 - \frac{2M}{\Sigma} \right) dt^2 + \frac{\Sigma}{\Delta} dr^2 - \frac{4aMr \sin^2 \theta}{\Sigma} dt d\phi + \Sigma d\theta^2 + \sin^2 \theta \left( r^2 + a^2 + a^2 \sin^2 \theta \frac{2Mr}{\Sigma} \right) d\phi^2, \quad (1)$$

where  $\Delta = r^2 - 2Mr + a^2$  and  $\Sigma = r^2 + a^2 \cos^2 \theta$ . We adopt the Hamilton-Jacobi formulation, the Hamilton-Jacobi equation reads

$$-\frac{\partial S}{\partial \tau} = \frac{1}{2} g^{\alpha\beta} \frac{\partial S}{\partial x^\alpha} \frac{\partial S}{\partial x^\beta}. \quad (2)$$

We know Kerr BH admits two obvious Killing vectors  $\partial_t$  and  $\partial_\phi$ , which correspond to two conserved charges, energy  $E$  and angular momentum  $L_z$ , thus for the mass point with mass  $\mu$ , we suppose the action function to be of the form

$$S = \frac{1}{2} \mu^2 \tau - Et + L_z \phi + S_r(r) + S_\theta(\theta), \quad (3)$$

which implies  $p_r = dS_r/dr$  and  $p_\theta = dS_\theta/d\theta$ . Inserting (3) into the Hamilton-Jacobi equation (2) and separating variables we have

$$S_r(r) = \pm \int dr \frac{1}{\Delta} \sqrt{R(r)}, \quad S_\theta(\theta) = \pm \int d\theta \sqrt{\Theta(\theta)}, \quad (4)$$

with

$$\begin{aligned} R(r) &\equiv [(r^2 + a^2)E - aL_z]^2 - \Delta [\mu^2 r^2 + (L_z - aE)^2 + Q], \\ \Theta(\theta) &\equiv Q + (L_z - aE)^2 - \mu^2 a^2 \cos^2 \theta - \frac{1}{\sin^2 \theta} [L_z - aE \sin^2 \theta]^2, \end{aligned} \quad (5)$$

where  $Q$  is a constant which is related with the separation constant  $C$  through  $Q = C - (L_z - aE)^2$ . Actually, the variable-separability of Hamilton-Jacobi equation in Kerr spacetime corresponds to a nontrivial symmetry which is described by a Killing tensor

$$K^{\mu\nu} = a^2 \cos^2 \theta g^{\mu\nu} + \frac{1}{\sin^2 \theta} \delta_\phi^\mu \delta_\phi^\nu + a^2 \sin^2 \theta \delta_t^\mu \delta_t^\nu - 2a \delta_t^\mu \delta_\phi^\nu + \delta_\theta^\mu \delta_\theta^\nu. \quad (6)$$

The Killing tensor satisfies the Killing equation  $\nabla_{(\lambda}K_{\mu\nu)} = 0$ , the bracket denotes symmetrization of the indices. This is a highly nontrivial symmetry which corresponds to the third conserved quantity—Carter constant  $Q$ —in addition to energy and angular momentum [58]. The explicit integration expression of coordinates can be obtained by setting the partial derivative of Hamilton-Jacobi function with respect to the constants of motion to be zero, that's to say the motions of particles in Kerr spacetime are integrable.

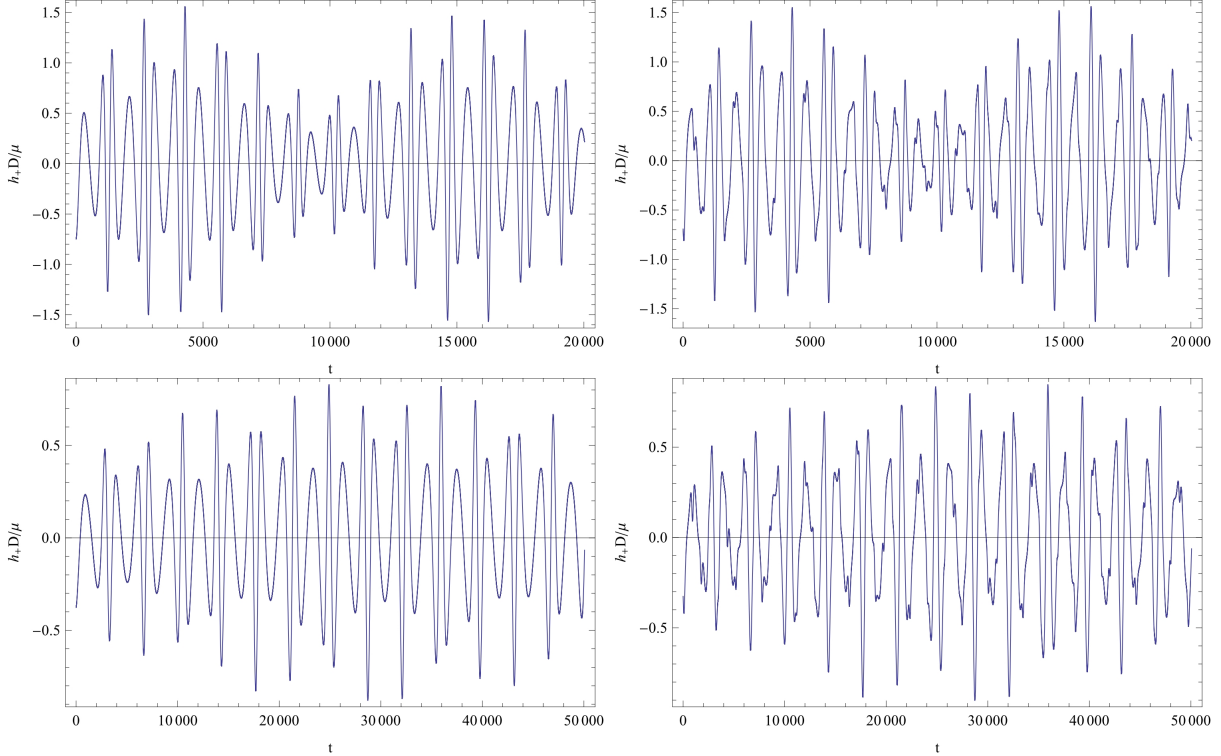


Figure 2:  $h_+$  waveforms of single and binary stars. For the binary the masses are taken as  $m_1 = M_\odot$  and  $m_2 = 1.1M_\odot$ . The mass of central SBH is set to be  $10^6M_\odot$ . The (external) orbit parameters of the upper two panels are set to be  $p(0) = 20M, e(0) = 0.3, a = 0.9$ , the internal orbit parameters of the upper right panel are set to be  $\tilde{p} = 5M, \tilde{e} = 0.2$ . The (external) orbit parameters of the lower two panels are set to be  $p(0) = 10M, e(0) = 0.3, a = 0.9$ , the internal orbit parameters of the lower right panel are set to be  $\tilde{p} = 3M, \tilde{e} = 0.3$ . One sees that extra burrs appear in the waveforms of B-EMRI compared to the single star revolving around a SBH.

With the above results, one now is able to give the geodesics of a mass point in Kerr spacetime

$$\begin{aligned}
 \Sigma \frac{dr}{d\tau} &= \pm \sqrt{V_r}, \\
 \Sigma \frac{d\theta}{d\tau} &= \pm \sqrt{V_\theta}, \\
 \Sigma \frac{d\phi}{d\tau} &= V_\phi, \\
 \Sigma \frac{dt}{d\tau} &= V_t,
 \end{aligned} \tag{7}$$

with

$$\begin{aligned}
V_r &= [E(r^2 + a^2) - L_z a]^2 - \Delta [\mu^2 r^2 + (L_z - aE)^2 + Q], \\
V_\theta &= Q - \cos^2 \theta \left[ a^2 (\mu^2 - E^2) + \frac{L_z^2}{\sin^2 \theta} \right], \\
V_\phi &= \frac{L_z}{\sin^2 \theta} - aE + \frac{a}{\Delta} [E(r^2 + a^2) - L_z a], \\
V_t &= a (L_z - aE \sin^2 \theta) + \frac{r^2 + a^2}{\Delta} [E(r^2 + a^2) - L_z a].
\end{aligned} \tag{8}$$

To solve the equations of geodesic motions (7) numerically, we introduce two angular variables  $\psi$  and  $\chi$  in place of  $r$  and  $\theta$  to avoid possible singularities.  $\psi$  is defined as

$$r = \frac{p}{1 + e \cos \psi}. \tag{9}$$

It's evident the periastron and apastron locate at  $r_p = \frac{p}{1+e}$  and  $r_a = \frac{p}{1-e}$ .  $\chi$  is defined as  $z = \cos^2 \theta = z_- \cos^2 \chi$ , where  $z_-$  is given by

$$\beta(z_+ - z)(z_- - z) = \beta z^2 - z [Q + L_z^2 + a^2(\mu^2 - E^2)] + Q, \tag{10}$$

with  $\beta = a^2(\mu^2 - E^2)$ . The parameter  $\chi$  ranges from 0 to  $2\pi$ . As  $\chi$  varies from 0 to  $2\pi$ ,  $\theta$  goes from one turning point  $\theta_{min}$  to the other  $\theta_{max}$  and back to  $\theta_{min}$ . We introduce an ‘‘inclination angle’’ to replace Carter constant  $Q = L_z^2 \tan^2 \iota$ . For  $\iota = 0$  or  $\pi$ ,  $Q$  equals to zero, from the geodesic equations (7) and (8) we know mass points remain on the equatorial plane at all times in this case. So  $Q = 0$  corresponds to the equatorial orbits while  $Q \neq 0$  corresponds to non-equatorial orbits. Expanding the radial potential as

$$V_r = (\mu^2 - E^2) (r_a - r) (r - r_p) (r - r_3) (r - r_4), \tag{11}$$

we find evolution equations for  $\psi$  and  $\chi$  to be of the form

$$\begin{aligned}
\frac{d\psi}{dt} &= \frac{\sqrt{\mu^2 - E^2} [(p - r_3(1 - e)) - e(p + r_3(1 - e) \cos \psi)]^{\frac{1}{2}} [(p - r_4(1 + e)) + e(p - r_4(1 + e) \cos \psi)]^{\frac{1}{2}}}{[\gamma + a^2 E z(\chi)] (1 - e^2)}, \\
\frac{d\chi}{dt} &= \frac{\sqrt{\beta [z_+ - z(\chi)]}}{\gamma + a^2 E z(\chi)},
\end{aligned} \tag{12}$$

where  $\gamma = E \left[ (r^2 + a^2)^2 / \Delta - a^2 \right] - \frac{2Mr a L_z}{\Delta}$ . Solving these equations allow us to know the positions of mass points at any time, which prepares us for calculating GWs in the following.

## 2.2 the GW waveform

In the weak-field situation, the metric can be decomposed as  $g_{\mu\nu} = \eta_{\mu\nu} + h_{\mu\nu}$ , where  $\eta_{\mu\nu}$  is the flat metric and  $h_{\mu\nu}$  is small perturbation. By introducing the traceless tensor  $\bar{h}^{\mu\nu} \equiv h^{\mu\nu} - (1/2)\eta^{\mu\nu}h$  with  $h = \eta^{\mu\nu}h_{\mu\nu}$ , then the Einstein equations can be recast to the form

$$\square \bar{h}^{\mu\nu} = -16\pi T^{\mu\nu}. \tag{13}$$

Here  $T^{\mu\nu}$  denotes the energy-momentum tensor of the source. In the slow motion limit, the GW is given by the quadrupole-octupole formula

$$\bar{h}^{jk} = \frac{2}{r} \left[ \ddot{I}^{jk} - 2n_i \dot{S}^{ijk} + n_i \ddot{M}^{ijk} \right]_{t'=t-r}, \tag{14}$$

with

$$\begin{aligned}
I^{jk}(t') &= \int x'^j x'^k T^{00}(t', \mathbf{x}') d^3 x', \\
S^{ijk}(t') &= \int x'^j x'^k T^{0i}(t', \mathbf{x}') d^3 x', \\
M^{ijk}(t') &= \int x'^i x'^j x'^k T^{00}(t', \mathbf{x}') d^3 x',
\end{aligned} \tag{15}$$

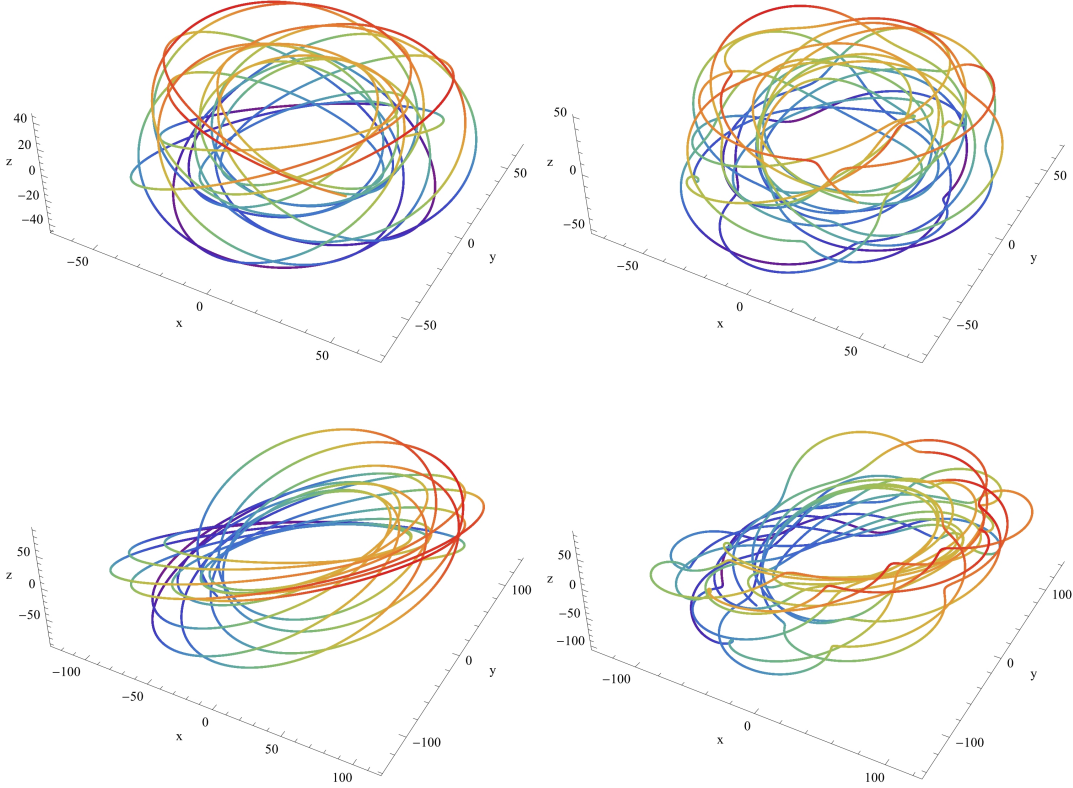


Figure 3: The orbits of compact objects generating the waveforms in Fig.2. For the binary we just display the orbit of one object of the two. The alignment of the panels correspond to the panels of waveforms in Fig.2.

being the mass quadrupole moment, current quadrupole moment and mass octupole moment respectively, and  $r^2 = \mathbf{x} \cdot \mathbf{x}$ ,  $\mathbf{n} = \mathbf{x}/r$ , where  $\mathbf{x}$  is the location of the observer.

In the NK prescription, a flat-space trajectory which is “equivalent” to a geodesic in Kerr spacetime is reconstructed by projecting the Boyer-Lindquist coordinates onto a fictitious spherical polar grid, the corresponding Cartesian coordinates are defined as

$$\begin{aligned} x_0 &= r \sin \theta \cos \phi, \\ y_0 &= r \sin \theta \sin \phi, \\ z_0 &= r \cos \theta. \end{aligned} \quad (16)$$

Then a particle moving along geodesic path in Kerr spacetime can be viewed as the particle moving along curved path in flat-space, thus it’s convenient for us to calculate GWs with Cartesian coordinates.

The expression (14) are valid for a general extended source in flat-space. For a single mass point with mass  $\mu$  the energy-momentum tensor in flat spacetime is given by

$$T^{\mu\nu}(t', \mathbf{x}') = \mu \int_{-\infty}^{\infty} \frac{dx_p'^{\mu}}{d\tau} \frac{dx_p'^{\nu}}{d\tau} \delta^4(x' - x'_p(\tau)) d\tau = \mu \left( \frac{d\tau}{dt'_p} \right)^2 \frac{dx_p'^{\mu}}{d\tau} \frac{dx_p'^{\nu}}{d\tau} \delta^3(\mathbf{x}' - \mathbf{x}'_p(t')). \quad (17)$$

For binary stars we know the energy-momentum tensor is the sum of two such terms. The momenta (15) now can be simplified to

$$\begin{aligned} I^{jk} &= \mu x_p'^j x_p'^k, \\ S^{ijk} &= v^i I^{jk}, \\ M^{ijk} &= x_p'^i I^{jk}. \end{aligned} \quad (18)$$

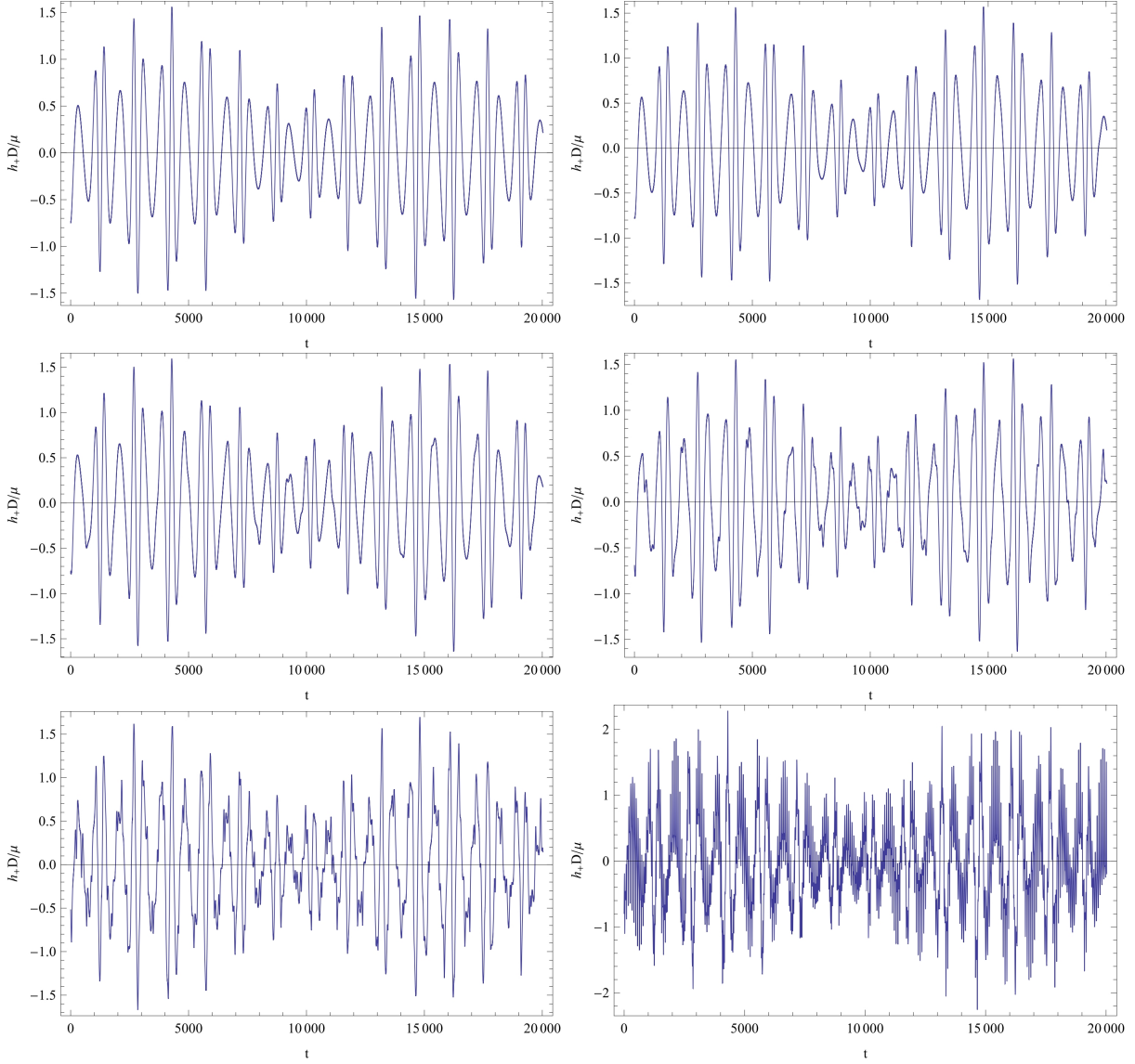


Figure 4: Comparisons between the EMRI  $h_+$  waveforms of single star (the upper left panel) and that of the binary with distinct semi-latus rectum  $\tilde{p}$  (the left five panels). The binary masses are fixed to be  $m_1 = M_\odot$  and  $m_2 = 1.1M_\odot$ , and mass of central SBH is  $10^6 M_\odot$ . The (external) orbit parameters are set to be  $p(0) = 10M$ ,  $e(0) = 0.3$ ,  $a = 0.9$ , the internal orbit parameters of the binary stars are set to be  $\tilde{e} = 0.2$ ,  $\theta_0 = \frac{\pi}{3}$  and  $\tilde{p} = 5M, 4M, 3M, 2M, M$  respectively.

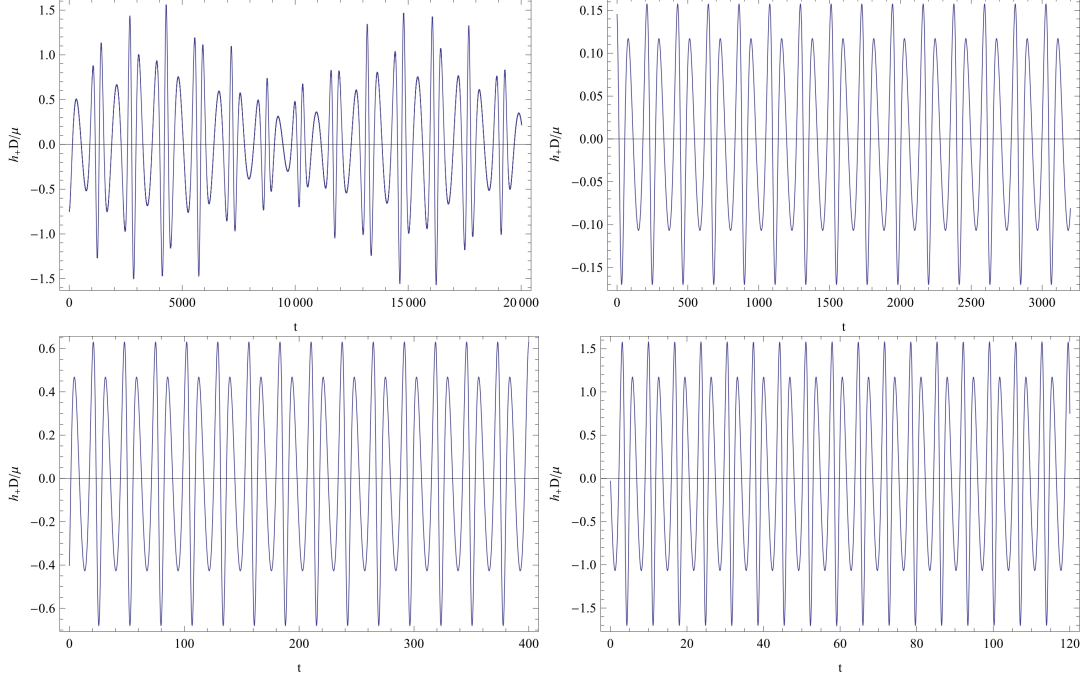


Figure 5: Comparisons of amplitude of GWs between pure external and pure internal motions of binary. The upper left panel displays the waveforms generated by external motions of center of mass revolving around SBH, the left three panels display the waveforms generated by pure internal motions of the binary revolving around each other. The external orbit parameters are taken to be identical with that in Fig.4. The semi-latus rectum of the internal orbits are set to be  $\tilde{p} = 2M, 0.5M, 0.2M$  respectively.

Substituting (18) into (14) one then obtains the GW generated by mass point.

In the standard transverse-traceless (TT) gauge, the waveform is given by the TT projection of (14). The orthonormal basis of spherical coordinates is defined as

$$\mathbf{e}_r = \frac{\partial}{\partial r}, \quad \mathbf{e}_\Theta = \frac{1}{r} \frac{\partial}{\partial \Theta}, \quad \mathbf{e}_\Phi = \frac{1}{r \sin \Theta} \frac{\partial}{\partial \Phi}, \quad (19)$$

where the angles  $\{\Theta, \Phi\}$  denote the observation point  $\bar{i}$ 's latitude and azimuth respectively. After TT projection the waveform is given by

$$h_{TT}^{jk} = \frac{1}{2} \begin{pmatrix} 0 & 0 & 0 \\ 0 & h^{\Theta\Theta} - h^{\Phi\Phi} & 2h^{\Theta\Phi} \\ 0 & 2h^{\Theta\Phi} & h^{\Phi\Phi} - h^{\Theta\Theta} \end{pmatrix}, \quad (20)$$

with

$$\begin{aligned} h^{\Theta\Theta} &= \cos^2 \Theta [h^{xx} \cos^2 \Phi + h^{xy} \sin 2\Phi + h^{yy} \sin^2 \Phi] + h^{zz} \sin^2 \Theta - \sin 2\Theta [h^{xz} \cos \Phi + h^{yz} \sin \Phi], \\ h^{\Phi\Theta} &= \cos \Theta \left[ -\frac{1}{2} h^{xx} \sin 2\Phi + h^{xy} \cos 2\Phi + \frac{1}{2} h^{yy} \sin 2\Phi \right] + \sin \Theta [h^{xz} \sin \Phi - h^{yz} \cos \Phi], \\ h^{\Phi\Phi} &= h^{xx} \sin^2 \Phi - h^{xy} \sin 2\Phi + h^{yy} \cos^2 \Phi. \end{aligned} \quad (21)$$

The usual ‘‘plus’’ and ‘‘cross’’ waveform polarizations are given by  $h^{\Theta\Theta} - h^{\Phi\Phi}$  and  $2h^{\Theta\Phi}$  respectively.

Due to the GW emissions, the compact objects will lose energy and angular momentum, although the amount of energy and angular momentum carried away by GWs is very small, the trajectory will alter accordingly, for a more precise study we consider backreaction of energy loss to the orbit. We study generic inclined-eccentric orbits of the center of mass of binary stars rather than just orbits on the equatorial plane. As we will see, since the amplitude of GW generated by internal motions of binary stars is small compared to that generated by external motions, we only consider the radiation reaction caused by the external motion of binary stars around the SBH while that



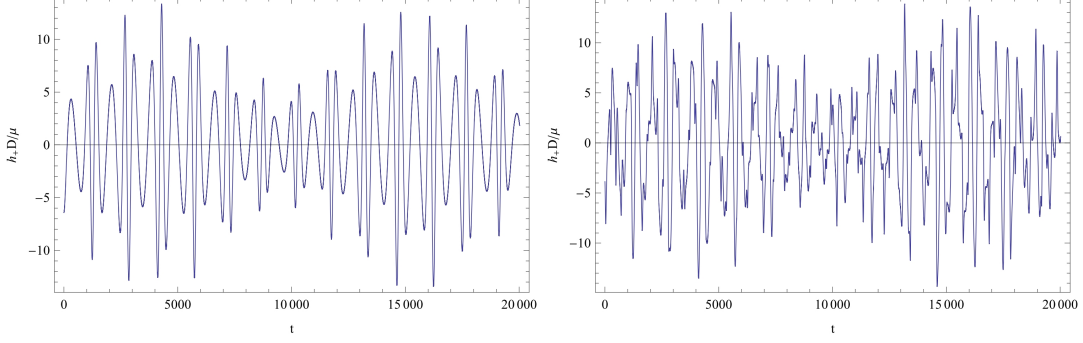


Figure 6: Waveforms of single compact object with mass equals to  $18M_\odot$  and binary with masses  $8M_\odot$  and  $10M_\odot$  revolving around central SBH with mass  $10^6 M_\odot$ . The (external) orbit parameters are set to be  $p(0) = 10M$ ,  $e(0) = 0.3$ , the internal motion parameters are set to be  $\tilde{p} = 2M$  and  $\tilde{e} = 0.2$ .

caused by the internal motion is neglected. We consider the flux of generic orbits to 2nd order post-Newtonian approximation [57]

$$\begin{aligned}
(\dot{E})_{2\text{PN}} &= -\frac{32}{5} \frac{\mu^2}{M^2} \left(\frac{M}{p}\right)^5 (1-e^2)^{3/2} \left[ g_1(e) - q \left(\frac{M}{p}\right)^{3/2} g_2(e) \cos \iota - \left(\frac{M}{p}\right) g_3(e) + \pi \left(\frac{M}{p}\right)^{3/2} g_4(e) \right. \\
&\quad \left. - \left(\frac{M}{p}\right)^2 g_5(e) + q^2 \left(\frac{M}{p}\right)^2 g_6(e) - \frac{527}{96} q^2 \left(\frac{M}{p}\right)^2 \sin^2 \iota \right], \\
(\dot{L}_z)_{2\text{PN}} &= -\frac{32}{5} \frac{\mu^2}{M} \left(\frac{M}{p}\right)^{7/2} (1-e^2)^{3/2} \left[ g_9(e) \cos \iota + q \left(\frac{M}{p}\right)^{3/2} \{g_{10}^a(e) - \cos^2 \iota g_{10}^b(e)\} - \left(\frac{M}{p}\right) g_{11}(e) \cos \iota \right. \\
&\quad \left. + \pi \left(\frac{M}{p}\right)^{3/2} g_{12}(e) \cos \iota - \left(\frac{M}{p}\right)^2 g_{13}(e) \cos \iota + q^2 \left(\frac{M}{p}\right)^2 \cos \iota \left( g_{14}(e) - \frac{45}{8} \sin^2 \iota \right) \right], \\
(\dot{Q})_{2\text{PN}} &= -\frac{64}{5} \frac{\mu^2}{M} \left(\frac{M}{p}\right)^{7/2} \sqrt{Q} \sin \iota (1-e^2)^{3/2} \left[ g_9(e) - q \left(\frac{M}{p}\right)^{3/2} \cos \iota g_{10}^b(e) - \left(\frac{M}{p}\right) g_{11}(e) \right. \\
&\quad \left. + \pi \left(\frac{M}{p}\right)^{3/2} g_{12}(e) - \left(\frac{M}{p}\right)^2 g_{13}(e) + q^2 \left(\frac{M}{p}\right)^2 \left( g_{14}(e) - \frac{45}{8} \sin^2 \iota \right) \right],
\end{aligned} \tag{22}$$

where  $q = a/M$ . We defer the expressions of the coefficients  $g_1(e) \sim g_{14}(e)$  to the Appendix. This expression of fluxes are the results of combining Tagoshi's [46], Shibata's [53] and Ryan's fluxes [55, 56]. Numerical analysis indicates that these results ameliorate the unphysical inspiral properties for nearly circular and polar orbits, such as the inspiral moves rapidly away from circularity for the trajectories near zero eccentricity  $e = 0$ , and there is discontinuity between trajectories with  $\iota$  slightly less than  $90^\circ$  and those slightly above  $90^\circ$ , etc., thus the fluxes (22) produce more physical reasonable results than previous ones. From (22), we obtain the evolution of eccentricity, semi-latus rectum and inclination angle

$$\begin{aligned}
\dot{e} &= \frac{\partial e}{\partial E} \dot{E} + \frac{\partial e}{\partial L_z} \dot{L}_z + \frac{\partial e}{\partial Q} \dot{Q}, \\
\dot{p} &= \frac{\partial p}{\partial E} \dot{E} + \frac{\partial p}{\partial L_z} \dot{L}_z + \frac{\partial p}{\partial Q} \dot{Q}, \\
\dot{\iota} &= \frac{\partial \iota}{\partial E} \dot{E} + \frac{\partial \iota}{\partial L_z} \dot{L}_z + \frac{\partial \iota}{\partial Q} \dot{Q}.
\end{aligned} \tag{23}$$

With all the results above, we are able to calculate the GW numerically with the NK method. In Figs.2, we exhibit the EMRI  $h_+$  waveforms of single and binary stars for two cases  $p = 10M$  and  $p = 20M$ . The orientation of the internal elliptic orbit plane is determined by the angles  $\theta_0 = \frac{\pi}{3}$ ,  $\phi_0 = \frac{\pi}{6}$ . The observer is supposed to be located

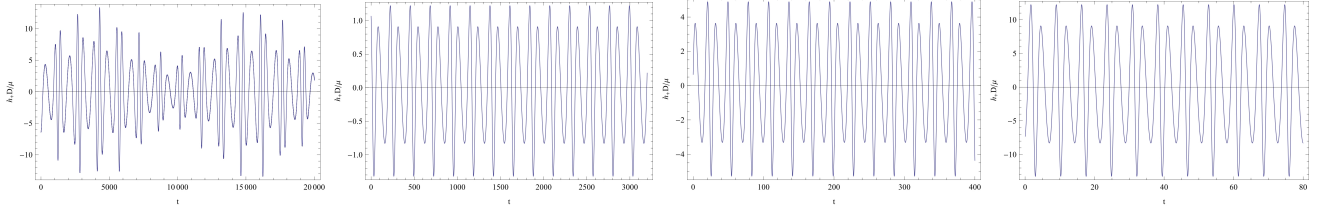


Figure 7: Comparisons of amplitudes of GWs generated by pure external (first panel) and that generated by pure internal motions (left three panels). The mass of central SBH is  $10^6 M_\odot$ , and the masses of the binary are  $8M_\odot$  and  $10M_\odot$ . The initial external motion parameters are set to be  $p(0) = 10M$ ,  $e(0) = 0.3$ , the internal motion parameters are fixed to be  $\tilde{e} = 0.2$  and  $\tilde{p} = 2M, 0.5M, 0.2M$ .

at  $r = D$  (100 Mpc in this case),  $\Theta = \frac{\pi}{3}$ ,  $\Phi = 0$ . From the figure we see that, the waveforms of the binary have the identical profile as that of the single star, but the waveforms of the binary have double spikes which are caused by the internal motion of the binary revolving around each other. We will analyze the waveforms in detail in the next section. In Fig.3, the orbits of one star in the binary system are displayed. It's evident to see that distinct waveforms emanate from distinct orbits of motions.

### 3 Analysis of the waveforms

In this section, we compare the waveforms of binary stars with that of single star in detail. Through calculating the mismatch we analyze the degree of match between the two waveforms. The overlap between two signals is defined as

$$\mathcal{O} = \langle x, h \rangle = 2 \int_0^{+\infty} \frac{\tilde{x}(f)\tilde{h}^*(f) + \tilde{x}^*(f)\tilde{h}(f)}{S_h(f)} df, \quad (24)$$

where  $\tilde{x}(f)$  and  $\tilde{h}(f)$  are the Fourier transformations of time-domain signals  $x(t)$  and  $h(t)$

$$\tilde{x}(f) = \int_{-\infty}^{\infty} x(t)e^{-i2\pi ft} dt, \quad \tilde{h}(f) = \int_{-\infty}^{\infty} h(t)e^{-i2\pi ft} dt. \quad (25)$$

$\tilde{x}^*(f)$  denote complex conjugate of  $\tilde{x}(f)$ , and  $S_h(f)$  in (24) is the one-sided noise power spectral density of LISA [59], which is useful for surveying the types of sources that can be detected by the LISA mission.

Mismatch of two singles is defined as

$$\Delta = 1 - \mathcal{O}. \quad (26)$$

There is a criterion that if two signals are distinguishable the mismatch  $\Delta$  and signal-noise-ratio (SNR)  $\rho$  should satisfy [60–64]

$$\Delta \geq \frac{1}{2\rho^2}, \quad (27)$$

where the SNR  $\rho$  is defined as  $\rho = \sqrt{\langle h, h \rangle}$  for a signal  $h$ . For LISA, the SNR is taken to be  $\rho = 20$  [16].

Fig.4 displays the change of waveforms according to semi-latus rectum  $\tilde{p}$  of binary internal elliptic orbit. We can see, compared with the waveform of single compact object (first panel in Fig.4) spikes appear in the waveforms of binary, and as  $\tilde{p}$  decreases more spikes appear. In other words, the smaller  $\tilde{p}$  is the larger the departure of binary waveforms from that of single star is. Thus it's straightforward to guess the mismatch of the two types of waveforms increases as  $\tilde{p}$  decreases, this is confirmed by the calculations of mismatch in frequency-domain in the following. In Fig.5, we compare the amplitudes of the GWs generated by pure external and that generated by pure internal motions. From the figure we see that, for the system composed of the central SBH with mass  $10^6 M_\odot$  and the binary with masses  $1M_\odot$  and  $1.1M_\odot$ , if  $p(0)$  is set to be  $10M$ , when the ratio of semi-latus rectums of internal and external orbits  $\tilde{p}/p$  is about 1 : 50, the amplitude of GWs generated by internal motions is comparable to that generated by external motions.

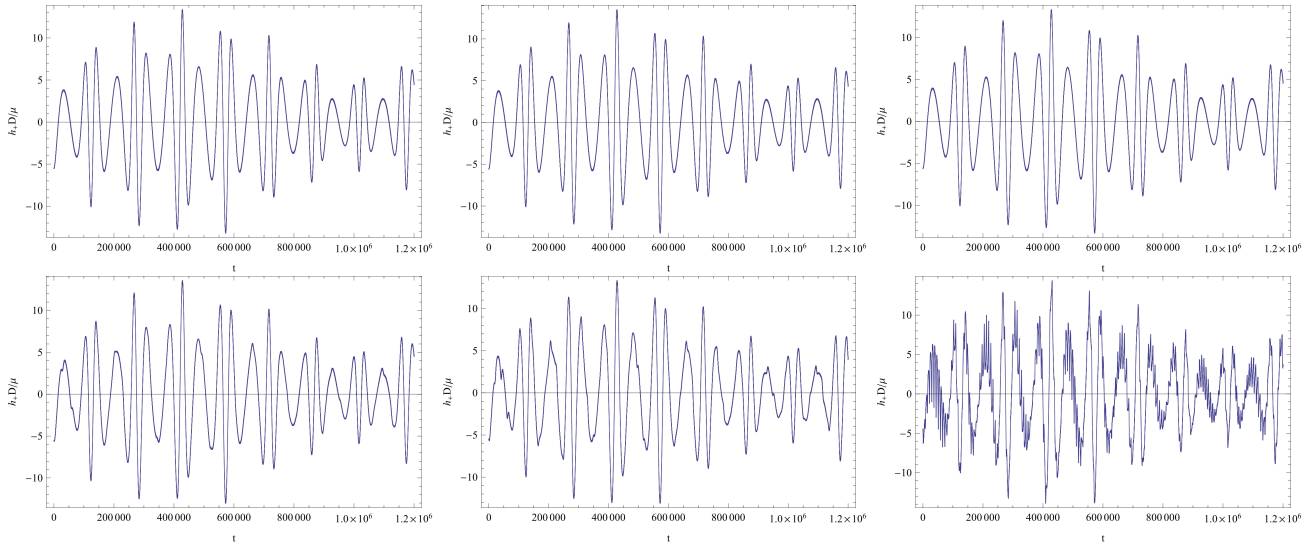


Figure 8: The  $h_+$  waveform emanating from single (first panel) and binary compact objects (left panels) revolving around central SBH with mass  $10^8 M_\odot$ . The masses of binary are set to be  $8M_\odot$  and  $10M_\odot$ . The external orbit parameters are set to be  $p(0) = 10M$ ,  $e(0) = 0.3$ . The internal motion parameters are set to be  $\tilde{e} = 0.2$  and  $\tilde{p} = 2M, M, 0.5M, 0.4M, 0.2M$ .

We fix the mass of central SBH to be  $10^6 M_\odot$  and increase the masses of binary to be  $8M_\odot$  and  $10M_\odot$ , Fig.6 displays the waveforms of this B-EMRIs. Compared with Fig.4 we see that spikes also appear in the waveforms of the binary, and the amplitudes of GWs increase with the masses of the binary as expected. We compare the amplitudes of GWs generated by pure external and pure internal motions for this case as well, as can be seen in Fig.7, we get similar results as above, i.e., when the ratio of semi-latus rectums  $\tilde{p}/p$  is about 1 : 50, the amplitude of GWs generated by internal motions is comparable to that generated by external motions.

Since there are a large number of SBHs with mass larger than  $10^6 M_\odot$  in the universe, we would like to calculate the GWs emanating from the binary revolving around heavier SBHs. Fig.8 displays the GWs emanating from the B-EMRIs composed of the central SBH with mass  $10^8 M_\odot$  and the binary with masses  $8M_\odot$  and  $10M_\odot$ . Similar to the above cases, due to period of binary internal motions decreases with  $\tilde{p}$ , more and more spikes appear as  $\tilde{p}$  decreases. Now, for the initial parameter  $p(0) = 10M$  if the ratio of semi-latus rectums  $\tilde{p}/p$  is about 3 : 10000 (see Fig.9), the amplitude of GWs generated by internal motions is comparable to that generated by external motions.

To analyze the waveforms of single and binary compact objects more accurately we calculate the mismatch of the two involved waveforms. The first two panels in Fig.10 display the variation of mismatch with  $\tilde{p}$ , it shows that as  $\tilde{p}$  decreases mismatch increases, which agrees with what we see in Fig.4. At first glance, one may expect the mismatch increases with  $\tilde{p}$  since larger  $\tilde{p}$  means greater departure from the orbits of single star. However, calculation shows as  $\tilde{p}$  increases mismatch decreases instead. This is because the GWs are functions of derivatives of coordinates, the smaller  $\tilde{p}$  is, the more greatly the coordinates of mass point change, and the more the departure of binary GW from that of single star is, and vice versa. We utilize the distinguishable criterion to judge whether the two involved waveforms are distinguishable. The dashed horizontal lines on the first two panels in Fig.10 denotes the indistinguishable bound corresponding to SNR  $\rho = 20$ . It can be seen easily that, for small enough  $\tilde{p}$  the GW signals of binary can be distinguished from that of single star, and that even if  $\tilde{p}$  is not small enough such that the amplitude of GW generated by pure internal motions is small and can be treated as perturbations of GWs generated by pure external motions, the two waveforms can be distinguished. The third panel of Fig.10 displays the variation of the mismatch with  $\theta_0$ , it shows that, as  $\theta_0$  increases mismatch first decreases and then increases, especially when  $\theta_0 = 0$  mismatch takes maximum value, i.e., when the rotation axis of the binary is parallel to the rotation axis of the SBH, the waveforms of binary are easiest distinguished from that of the single star.

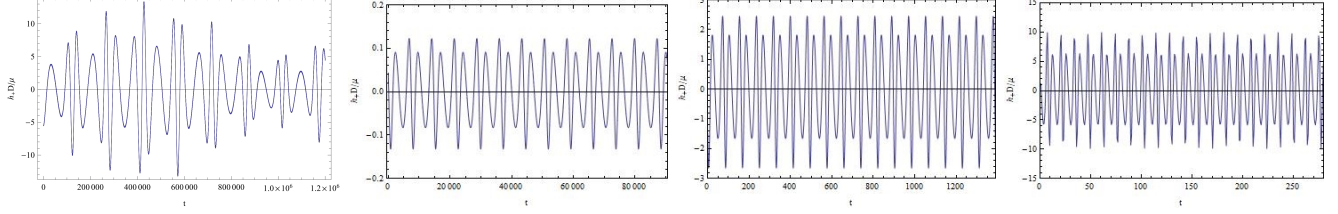


Figure 9: Comparisons of amplitudes of GWs generated by pure external (first panel) and pure internal (left three panels) motions of binary in Fig.8, the semi-latus rectum of internal orbits are set to be  $\tilde{p} = 0.2M, 0.01M, 0.003M$  respectively.

## 4 Discussion and Conclusion

In this paper we study the GWs emanating from B-EMRIs which is composed of a central SBH and binary revolving around it. The SBH is supposed to be Kerr. We solve the GW equations by taking into account the mass quadrupole, mass octupole and current quadrupole moments of the source. For the radiation reaction we take the hybrid 2nd order post-Newtonian approximation which is applicable to generic inclined-eccentric orbits. We plot the GW waveforms of B-EMRIs and compare the waveforms of B-EMRIs with that of EMRIs of single star. The results show that, compared to the waveforms generated by single stellar-mass compact object the ones generated by binary compact objects exhibit double spikes or multi spikes. The spikes are caused by internal motions of the binary. The smaller  $\tilde{p}$  is, the more and larger the spikes are. We compare the amplitudes of GWs generated by pure internal motions with that generated by pure external motions. Calculations show that for the B-EMRIs composed of central SBH with  $M = 10^6 M_\odot$  and the binary with  $m_1 = M_\odot, m_2 = 1.1M_\odot$  or  $m_1 = 8M_\odot, m_2 = 10M_\odot$ , if the ratio of semi-latus rectums  $\tilde{p}/p$  is about 1 : 50, the amplitudes of GWs generated by pure internal motions is comparable to that generated by pure external motions. For the B-EMRIs composed of central SBH with  $M = 10^8 M_\odot$  and the binary with  $m_1 = 8M_\odot, m_2 = 10M_\odot$ , if the ratio  $\tilde{p}/p$  is about 3 : 10000, the amplitudes of GWs generated by pure internal motions is comparable to that generated by pure external motions.

We calculate the mismatch of two waveforms, the results show that, as  $\tilde{p}$  decreases the mismatch increases, which agrees with the waveforms show us. This is a little counter-intuitive since it seems larger  $\tilde{p}$  means greater departure from the orbits of single star. Actually, since GWs are functions of derivatives of coordinates, the larger  $\tilde{p}$  is the smoother the orbit is, and the smaller the change rate of coordinates is, so larger  $\tilde{p}$  corresponds to less departure of waveforms from that of single star. Applying the distinguishable criterion of two waveforms we find if  $\tilde{p}$  is small enough the waveforms of binary are distinguishable from that of single star, even if  $\tilde{p}$  is not too small and the GWs generated by pure internal motions can be viewed as perturbations of the GWs generated by pure external motions, the waveforms of B-EMRIs can be distinguishable from that of single star EMRIs. We also calculate the mismatch of two waveforms with different  $\theta_0$  which is the angle between the surface of binary internal elliptic orbit and the horizontal surface, the results show that when  $\theta_0 = 0$  mismatch takes maximum value, which means when the rotation axis of the binary is parallel to the rotation axis of the SBH, the waveforms of binary are in the most striking contrast from that of single star, and thus is the most beneficial position for observation to distinguish the GWs from EMRIs of single star and binary stars.

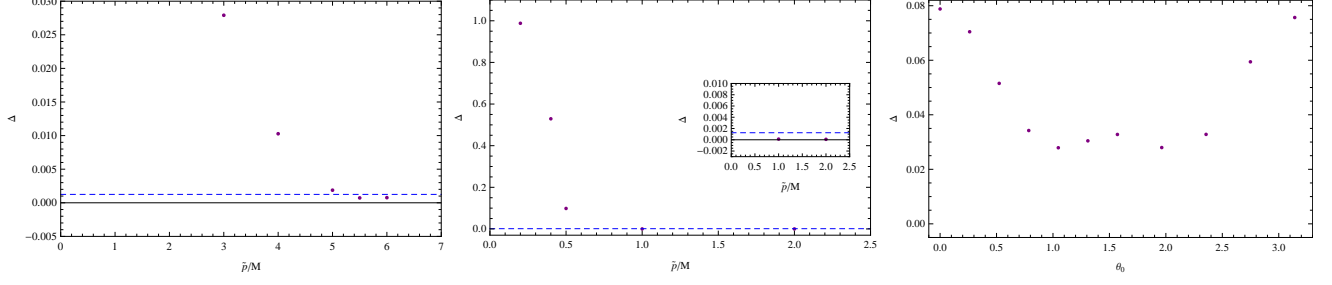


Figure 10: Mismatch  $\Delta$  as functions of  $\tilde{p}$  or  $\theta_0$ . For the left panel the parameters are taken to be  $p(0) = 10M$ ,  $e(0) = 0.3$ ,  $a = 0.9$ ,  $\tilde{e} = 0.2$ ,  $\theta_0 = \frac{\pi}{3}$ ,  $m_2 = 1.1M_\odot$ ,  $m_1 = M_\odot$ , and  $\tilde{p} = 3M, 4M, 5M, 5.5M, 6M$  respectively. For the middle panel the parameters are fixed to be  $p(0) = 10M$ ,  $e(0) = 0.3$ ,  $a = 0.9$ ,  $\tilde{e} = 0.2$ ,  $\theta_0 = \frac{\pi}{3}$ ,  $m_2 = 10M_\odot$ ,  $m_1 = 8M_\odot$  and  $\tilde{p} = 0.2M, 0.4M, 0.5M, M, 2M$  respectively. For the right panel the parameters are fixed as  $p(0) = 10M$ ,  $e(0) = 0.3$ ,  $a = 0.9$ ,  $\tilde{p} = 3M$ ,  $\tilde{e} = 0.2$ ,  $m_2 = 1.1M_\odot$ ,  $m_1 = M_\odot$ , and  $\theta_0 = \frac{\pi}{12}, \frac{\pi}{6}, \frac{\pi}{4}, \frac{\pi}{3}, \frac{5\pi}{12}, \frac{\pi}{2}$  respectively.

## Appendix

The  $e$ -dependent coefficients appear in Eq.(22) are given by

$$\begin{aligned}
g_1(e) &= 1 + \frac{73}{24}e^2 + \frac{37}{96}e^4, & g_2(e) &= \frac{73}{12} + \frac{823}{24}e^2 + \frac{949}{32}e^4 + \frac{491}{192}e^6, \\
g_3(e) &= \frac{1247}{336} + \frac{9181}{672}e^2, & g_4(e) &= 4 + \frac{1375}{48}e^2, \\
g_5(e) &= \frac{44711}{9072} + \frac{172157}{2592}e^2, & g_6(e) &= \frac{33}{16} + \frac{359}{32}e^2, & g_9(e) &= 1 + \frac{7}{8}e^2, \\
g_{10}^a(e) &= \frac{61}{24} + \frac{63}{8}e^2 + \frac{95}{64}e^4, & g_{10}^b(e) &= \frac{61}{8} + \frac{91}{4}e^2 + \frac{461}{64}e^4. \\
g_{11}(e) &= \frac{1247}{336} + \frac{425}{336}e^2, & g_{12}(e) &= 4 + \frac{97}{8}e^2, \\
g_{13}(e) &= \frac{44711}{9072} + \frac{302893}{6048}e^2, & g_{14}(e) &= \frac{33}{16} + \frac{95}{16}e^2, \\
g_{15}(e) &= \frac{8191}{672} + \frac{48361}{1344}e^2, & g_{16}(e) &= \frac{417}{56} - \frac{37241}{672}e^2.
\end{aligned}$$

## Acknowledgment

This work is supported by the National Key R&D Program of China (no.2021YFC2203002), the National Natural Science Foundation of China Grants Nos. 12275106 and 12235019, and Natural Science Foundation of Shandong Province Nos.ZR2023MA014.

## References

- [1] K. Akiyama *et al.* [Event Horizon Telescope], *First M87 Event Horizon Telescope Results. VI. The Shadow and Mass of the Central Black Hole*, *Astrophys. J. Lett.* **875**, no.1, (2019) L6 [arXiv:1906.11243 [astro-ph.GA]].
- [2] K. Akiyama *et al.* [Event Horizon Telescope], *First Sagittarius A\* Event Horizon Telescope Results. VI. Testing the Black Hole Metric*, *Astrophys. J. Lett.* **930**, no.2, L17 (2022).
- [3] B. P. Abbott *et al.* [LIGO Scientific and Virgo], *Observation of Gravitational Waves from a Binary Black Hole Merger*, *Phys. Rev. Lett.* **116**, no.6, 061102 (2016) [arXiv:1602.03837 [gr-qc]].

- [4] B. P. Abbott *et al.* [LIGO Scientific and Virgo], *GW151226: Observation of Gravitational Waves from a 22-Solar-Mass Binary Black Hole Coalescence*, *Phys. Rev. Lett.* **116**, no.24, 241103 (2016) [arXiv:1606.04855 [gr-qc]].
- [5] S. Sigurdsson, *Estimating the detectable rate of capture of stellar mass black holes by massive central black holes in normal galaxies*, *Class. Quant. Grav.* **14**, 1425-1429 (1997) [arXiv:astro-ph/9701079 [astro-ph]].
- [6] S. Sigurdsson and M. J. Rees, *Capture of stellar mass compact objects by massive black holes in galactic cusps*, *Mon. Not. Roy. Astron. Soc.* **284**, 318 (1997) [arXiv:astro-ph/9608093 [astro-ph]].
- [7] S. A. Hughes, *Evolution of circular, nonequatorial orbits of Kerr black holes due to gravitational wave emission. II. Inspiral trajectories and gravitational wave forms*, *Phys. Rev. D* **64**, 064004 (2001) [erratum: *Phys. Rev. D* **88**, no.10, 109902 (2013)] [arXiv:gr-qc/0104041 [gr-qc]].
- [8] K. Glampedakis and D. Kennefick, *Zoom and whirl: Eccentric equatorial orbits around spinning black holes and their evolution under gravitational radiation reaction*, *Phys. Rev. D* **66**, 044002 (2002) [arXiv:gr-qc/0203086 [gr-qc]].
- [9] P. Gupta, L. Speri, B. Bonga, A. J. K. Chua and T. Tanaka, *Modeling transient resonances in extreme-mass-ratio inspirals*, *Phys. Rev. D* **106**, no.10, 104001 (2022) [arXiv:2205.04808 [gr-qc]].
- [10] L. Polcar, G. Lukes-Gerakopoulos and V. Witzany, *Extreme mass ratio inspirals into black holes surrounded by matter*, *Phys. Rev. D* **106**, no.4, 044069 (2022) [arXiv:2205.08516 [gr-qc]].
- [11] C. Munna and C. R. Evans, *Post-Newtonian expansion of the spin-precession invariant for eccentric-orbit nonspinning extreme-mass-ratio inspirals to 9PN and  $\epsilon_{16}$* , *Phys. Rev. D* **106**, no.4, 044058 (2022) [arXiv:2206.04085 [gr-qc]].
- [12] M. Kerachian, L. Polcar, V. Skoupý, C. Efthymiopoulos and G. Lukes-Gerakopoulos, *Action-angle formalism for extreme mass ratio inspirals in Kerr spacetime*, *Phys. Rev. D* **108**, no.4, 044004 (2023) [arXiv:2301.08150 [gr-qc]].
- [13] T. Takahashi, H. Omiya and T. Tanaka, *Evolution of binary systems accompanying axion clouds in extreme mass ratio inspirals*, *Phys. Rev. D* **107**, no.10, 103020 (2023) [arXiv:2301.13213 [gr-qc]].
- [14] L. M. Burko and G. Khanna, *Self-force gravitational waveforms for extreme and intermediate mass ratio inspirals. II: Importance of the second-order dissipative effect*, *Phys. Rev. D* **88**, no.2, 024002 (2013) [arXiv:1304.5296 [gr-qc]].
- [15] K. Glampedakis, *Extreme mass ratio inspirals: LISA's unique probe of black hole gravity*, *Class. Quant. Grav.* **22**, S605-S659 (2005) [arXiv:gr-qc/0509024 [gr-qc]].
- [16] S. Babak, J. Gair, A. Sesana, E. Barausse, C. F. Sopuerta, C. P. L. Berry, E. Berti, P. Amaro-Seoane, A. Petiteau and A. Klein, *Science with the space-based interferometer LISA. V: Extreme mass-ratio inspirals*, *Phys. Rev. D* **95**, no.10, 103012 (2017) [arXiv:1703.09722 [gr-qc]].
- [17] C. Munna and C. R. Evans, *Eccentric-orbit extreme-mass-ratio-inspiral radiation: Analytic forms of leading-logarithm and subleading-logarithm flux terms at high PN orders*, *Phys. Rev. D* **100**, no.10, 104060 (2019) [arXiv:1909.05877 [gr-qc]].
- [18] T. G. Zi, J. D. Zhang, H. M. Fan, X. T. Zhang, Y. M. Hu, C. Shi and J. Mei, *Science with the TianQin Observatory: Preliminary results on testing the no-hair theorem with extreme mass ratio inspirals*, *Phys. Rev. D* **104**, no.6, 064008 (2021) [arXiv:2104.06047 [gr-qc]].
- [19] K. Destounis, A. Kulathingal, K. D. Kokkotas and G. O. Papadopoulos, *Gravitational-wave imprints of compact and galactic-scale environments in extreme-mass-ratio binaries*, *Phys. Rev. D* **107**, no.8, 084027 (2023) [arXiv:2210.09357 [gr-qc]].
- [20] T. Zi and P. C. Li, *Probing the tidal deformability of the central object with analytic kludge waveforms of an extreme-mass-ratio inspiral*, *Phys. Rev. D* **108**, no.2, 024018 (2023) [arXiv:2303.16610 [gr-qc]].
- [21] L. Barack and C. Cutler, *LISA capture sources: Approximate waveforms, signal-to-noise ratios, and parameter estimation accuracy*, *Phys. Rev. D* **69**, 082005 (2004) [arXiv:gr-qc/0310125 [gr-qc]].
- [22] T. Zi and P. C. Li, *Gravitational waves from extreme-mass-ratio inspirals around a hairy Kerr black hole*, *Phys. Rev. D* **108**, no.8, 084001 (2023) [arXiv:2306.02683 [gr-qc]].
- [23] N. Dai, Y. Gong, Y. Zhao and T. Jiang, *Extreme mass ratio inspirals in galaxies with dark matter halos*, [arXiv:2301.05088 [gr-qc]].
- [24] Z. Pan, H. Yang, L. Bernard and B. Bonga, *Resonant dynamics of extreme mass-ratio inspirals in a perturbed Kerr spacetime*, *Phys. Rev. D* **108**, no.10, 104026 (2023) [arXiv:2306.06576 [gr-qc]].
- [25] C. Zhang, Y. Gong, D. Liang and B. Wang, *Gravitational waves from eccentric extreme mass-ratio inspirals as probes of scalar fields* *JCAP* **06**, 054 (2023) [arXiv:2210.11121 [gr-qc]].
- [26] D. Liang, R. Xu, Z. F. Mai and L. Shao, *Probing vector hair of black holes with extreme-mass-ratio inspirals* *Phys. Rev. D* **107**, no.4, 044053 (2023) [arXiv:2212.09346 [gr-qc]].
- [27] C. M. Will, *Gravitational Radiation from Binary Systems in Alternative Metric Theories of Gravity: Dipole Radiation and the Binary Pulsar*, *Astrophys. J.* **214**, 826-839 (1977)
- [28] C. M. Will and H. W. Zaglauer, *Gravitational Radiation, Close Binary Systems, and the Brans-dicke Theory of Gravity*, *Astrophys. J.* **346**, 366 (1989)
- [29] E. Barausse and K. Yagi, *Gravitation-Wave Emission in Shift-Symmetric Horndeski Theories*, *Phys. Rev. Lett.* **115**, no.21, 211105 (2015) [arXiv:1509.04539 [gr-qc]].
- [30] R. Xu, Y. Gao and L. Shao, *Neutron stars in massive scalar-Gauss-Bonnet gravity: Spherical structure and time-independent perturbations*, *Phys. Rev. D* **105**, no.2, 024003 (2022) [arXiv:2111.06561 [gr-qc]].
- [31] J. Tan, J. d. Zhang, H. M. Fan and J. Mei, *Constraining the EdGB Theory with Extreme Mass-Ratio Inspirals*, [arXiv:2402.05752 [gr-qc]].

- [32] J. Gair and N. Yunes, *Approximate Waveforms for Extreme-Mass-Ratio Inspirals in Modified Gravity Spacetimes*, *Phys. Rev. D* **84**, 064016 (2011) [arXiv:1106.6313 [gr-qc]].
- [33] M. Rahman, S. Kumar and A. Bhattacharyya, *Gravitational wave from extreme mass-ratio inspirals as a probe of extra dimensions*, *JCAP* **01**, 046 (2023) doi:10.1088/1475-7516/2023/01/046 [arXiv:2212.01404 [gr-qc]].
- [34] T. Zi, Z. Zhou, H. T. Wang, P. C. Li, J. d. Zhang and B. Chen, *Analytic kludge waveforms for extreme-mass-ratio inspirals of a charged object around a Kerr-Newman black hole*, *Phys. Rev. D* **107**, no.2, 023005 (2023) [arXiv:2205.00425 [gr-qc]].
- [35] S. C. Yang, R. D. Tang, X. Y. Zhong, Y. H. Zhang and W. B. Han, *Recognizing the constitution of small bodies in extreme-mass-ratio inspirals by gravitational waves*, [arXiv:2209.01110 [gr-qc]].
- [36] C. Zhang and Y. Gong, *Detecting electric charge with extreme mass ratio inspirals*, *Phys. Rev. D* **105**, no.12, 124046 (2022) [arXiv:2204.08881 [gr-qc]].
- [37] L. V. Drummond, A. G. Hanselman, D. R. Becker and S. A. Hughes, *Extreme mass-ratio inspiral of a spinning body into a Kerr black hole I: Evolution along generic trajectories*, [arXiv:2305.08919 [gr-qc]].
- [38] Y. Mino, M. Shibata and T. Tanaka, *Gravitational waves induced by a spinning particle falling into a rotating black hole*, *Phys. Rev. D* **53**, 622-634 (1996) [erratum: *Phys. Rev. D* **59**, 047502 (1999)]
- [39] B. Toshmatov, O. Rahimov, B. Ahmedov and D. Malafarina, *Motion of spinning particles in non asymptotically flat spacetimes*, *Eur. Phys. J. C* **80**, no.7, 675 (2020) [arXiv:2003.09227 [gr-qc]].
- [40] G. A. Piovano, A. Maselli and P. Pani, *Extreme mass ratio inspirals with spinning secondary: a detailed study of equatorial circular motion*, *Phys. Rev. D* **102**, no.2, 024041 (2020) [arXiv:2004.02654 [gr-qc]].
- [41] S. Drasco and S. A. Hughes, *Gravitational wave snapshots of generic extreme mass ratio inspirals*, *Phys. Rev. D* **73**, no.2, 024027 (2006) [erratum: *Phys. Rev. D* **88**, no.10, 109905 (2013); erratum: *Phys. Rev. D* **90**, no.10, 109905 (2014)] [arXiv:gr-qc/0509101 [gr-qc]].
- [42] S. A. Hughes, *The Evolution of circular, nonequatorial orbits of Kerr black holes due to gravitational wave emission*, *Phys. Rev. D* **61**, no.8, 084004 (2000) [erratum: *Phys. Rev. D* **63**, no.4, 049902 (2001); erratum: *Phys. Rev. D* **65**, no.6, 069902 (2002); erratum: *Phys. Rev. D* **67**, no.8, 089901 (2003); erratum: *Phys. Rev. D* **78**, no.10, 109902 (2008); erratum: *Phys. Rev. D* **90**, no.10, 109904 (2014)] [arXiv:gr-qc/9910091 [gr-qc]].
- [43] C. Cutler, D. Kennefick and E. Poisson, *Gravitational radiation reaction for bound motion around a Schwarzschild black hole*, *Phys. Rev. D* **50**, 3816-3835 (1994).
- [44] T. Tanaka, M. Shibata, M. Sasaki, H. Tagoshi and T. Nakamura, *Gravitational wave induced by a particle orbiting around a Schwarzschild black hole*, *Prog. Theor. Phys.* **90**, 65-84 (1993).
- [45] M. Shibata, *Gravitational Waves Induced by a Particle Orbiting around a Rotating Black Hole: Effect of Orbital Precession*,
- [46] H. Tagoshi, *Post Newtonian expansion of gravitational waves from a particle in slightly eccentric orbit around a rotating black hole*, *Prog. Theor. Phys.* **93**, 307-333 (1995) [erratum: *Prog. Theor. Phys.* **118**, 577-579 (2007)]
- [47] E. Poisson, *Gravitational radiation from a particle in circular orbit around a black hole. 1: Analytical results for the nonrotating case*, *Phys. Rev. D* **47**, 1497-1510 (1993).
- [48] C. Cutler, E. Poisson, G. J. Sussman and L. S. Finn, *Gravitational radiation from a particle in circular orbit around a black hole. 2: Numerical results for the nonrotating case*, *Phys. Rev. D* **47**, 1511-1518 (1993).
- [49] T. Apostolatos, D. Kennefick, E. Poisson and A. Ori, *Gravitational radiation from a particle in circular orbit around a black hole. 3: Stability of circular orbits under radiation reaction*, *Phys. Rev. D* **47**, 5376-5388 (1993).
- [50] E. Poisson, *Gravitational radiation from a particle in circular orbit around a black hole. 4: Analytical results for the slowly rotating case*, *Phys. Rev. D* **48**, 1860-1863 (1993).
- [51] E. Poisson and M. Sasaki, *Gravitational radiation from a particle in circular orbit around a black hole. 5: Black hole absorption and tail corrections*, *Phys. Rev. D* **51**, 5753-5767 (1995) [arXiv:gr-qc/9412027 [gr-qc]].
- [52] H. Tagoshi and M. Sasaki, *Post Newtonian expansion of gravitational waves from a particle in circular orbit around a Schwarzschild black hole*, *Prog. Theor. Phys.* **92**, 745-772 (1994) [arXiv:gr-qc/9405062 [gr-qc]].
- [53] M. Shibata, M. Sasaki, H. Tagoshi and T. Tanaka, *Gravitational waves from a particle orbiting around a rotating black hole: PostNewtonian expansion*, *Phys. Rev. D* **51**, 1646-1663 (1995) [arXiv:gr-qc/9409054 [gr-qc]].
- [54] S. Babak, H. Fang, J. R. Gair, K. Glampedakis and S. A. Hughes, *'Kludge' gravitational waveforms for a test-body orbiting a Kerr black hole*, *Phys. Rev. D* **75**, 024005 (2007) [erratum: *Phys. Rev. D* **77**, 04990 (2008)] [arXiv:gr-qc/0607007 [gr-qc]].
- [55] F. D. Ryan, *Effect of gravitational radiation reaction on circular orbits around a spinning black hole*, *Phys. Rev. D* **52**, R3159-R3162 (1995) [arXiv:gr-qc/9506023 [gr-qc]].
- [56] F. D. Ryan, *Effect of gravitational radiation reaction on nonequatorial orbits around a Kerr black hole*, *Phys. Rev. D* **53**, 3064-3069 (1996) [arXiv:gr-qc/9511062 [gr-qc]].
- [57] J. R. Gair and K. Glampedakis, *Improved approximate inspirals of test-bodies into Kerr black holes*, *Phys. Rev. D* **73**, 064037 (2006) [arXiv:gr-qc/0510129 [gr-qc]].
- [58] B. Carter, *Axisymmetric Black Hole Has Only Two Degrees of Freedom*, *Phys. Rev. Lett.* **26**, 331-333 (1971).
- [59] T. Robson, N. J. Cornish and C. Liu, *The construction and use of LISA sensitivity curves*, *Class. Quant. Grav.* **36**, no.10, 105011 (2019) [arXiv:1803.01944 [astro-ph.HE]].

- [60] L. V. Drummond, P. Lynch, A. G. Hanselman, D. R. Becker and S. A. Hughes, *Extreme mass-ratio inspiral and waveforms for a spinning body into a Kerr black hole via osculating geodesics and near-identity transformations*, [arXiv:2310.08438 [gr-qc]].
- [61] H. Yu, J. Roulet, T. Venumadhav, B. Zackay and M. Zaldarriaga, *Accurate and efficient waveform model for precessing binary black holes*, *Phys. Rev. D* **108**, no.6, 064059 (2023) [arXiv:2306.08774 [gr-qc]].
- [62] M. Pürrer, *Frequency domain reduced order models for gravitational waves from aligned-spin compact binaries* *Class. Quant. Grav.* **31**, no.19, 195010 (2014) [arXiv:1402.4146 [gr-qc]].
- [63] F. Ohme, *Analytical meets numerical relativity - status of complete gravitational waveform models for binary black holes*, *Class. Quant. Grav.* **29**, 124002 (2012) [arXiv:1111.3737 [gr-qc]].
- [64] P. Lynch, M. van de Meent and N. Warburton, *Eccentric self-forced inspirals into a rotating black hole*, *Class. Quant. Grav.* **39**, no.14, 145004 (2022) [arXiv:2112.05651 [gr-qc]].